Macroscopic network circulation for planar graphs

Fariba Ariaei*, Zahra Askarzadeh*, Yongxin Chen, Tryphon T. Georgiou

Abstract—The analysis of networks, aimed at suitably defined functionality, often focuses on partitions into subnetworks that capture desired features. Chief among the relevant concepts is a 2-partition; this underlies the classical Cheeger inequality and highlights a "constriction" (bottleneck) that limits accessibility between the respective parts of the network. In a similar spirit, we explore a notion of global circulation which necessitates a concept of a 3-partition that exposes this macroscopic feature of network flows. Graph circulation is often present in transportation networks as well as in certain biological networks. We introduce a notion of circulation for general graphs and then focus on planar graphs. For the case of the latter we explain that a scalar potential characterizes circulation in complete analogy with the curl of planar vector fields and we present an algorithm for determining values of the potential and, hence, quantify circulation. We then discuss alternative notions of circulation, explain how these may depend on graph embedding, draw parallels between networks and Helmholtz-Hodge decomposition of vector fields, and conclude with a suggestive application of the framework in detecting abnormalities in cardiac circulatory physiology.

I. INTRODUCTION

Time asymmetry of traffic flow in city streets is unmistakable, as it flows in one direction around city squares and one-way in many city streets as well. Yet, from a macroscopic vantage point, circulation may or may not be evident. Flux from one part of town to another may average out with flux in the opposite direction. When this is not the case, it is of interest to identify the nature and to quantify any large scale imbalance in circulation. Likewise, in another example that motivated this work, it is of interest to detect circulatory action potentials in the heart electrical conduction system [1], [2]. Such large scale imbalance patterns, peered via a collection of sensors, underly self-sustaining cardiac rhythm abnormalities¹. Thus, herein, we seek to define and identify macroscopic circulation in a network/graph that captures flow asymmetry at large scale.

F. Ariaei, Z. Askarzadeh, and T. T. Georgiou are with the Department of Mechanical and Aerospace Engineering, University of California, Irvine, CA; zaskarza@uci.edu, fariaei@uci.edu, tryphon@uci.edu

Y. Chen is with the School of Aerospace Engineering, Georgia Institute of Technology, Atlanta, GA 30332; yongchen@gatech.edu

The mathematical setting we use to model flows on graphs is that of a stationary discrete-time Markov model, where the probability flux represents a vector field on the network of the nodes and edges of a Markov chain. In this setting, the famous Cheeger constant relates the likelihood of transitioning between two parts in a 2-partition of the nodes and quantifies bottlenecks that impede mixing. In a similar manner, contemplating the elements of circulatory imbalance, we are led naturally to a 3-partition of the network; tell-tale signs of circulatory asymmetry requires partitioning with at least three parts.

Graph theory has impacted many fields in mathematics, physics, network science, biology, medicine, and engineering [4]–[6]. Applications relate to clustering, community detection, parallel computation, and so on, and in these, graph partitioning often plays a key role. For instance, local [7], [8] and global [9] partitioning of undirected and directed graphs in different contexts, partitioning having sparsest cuts [10], and various generalizations of the classical Cheeger inequality [11], all provided enabling new insights and techniques for applications. In the recent years, Helmholtz-Hodge decomposition and higher order graph Laplacians have also been used as powerful tools to characterize structural properties of flow fields on graphs, and to describe the dynamics of processes on networks [12]-[14]. Yet the concept of circulation discussed at present does not appear to have been studied at any length. Thus, a main contribution of the present work is motivate and study circulation in graphs and the topology of corresponding partitions. Further, a computational framework is developed that applies to embedded planar graphs; for general graphs macroscopic circulation and the corresponding graph partitioning remain challenging combinatorial problems.

The structure of the paper is as follows. Section II discusses probability currents and flow fields on graphs. Section III discusses the concept of macroscopic circulation. Section IV focuses on planar graphs and the relevant decomposition of flows. Section V covers an algorithm for calculating the scalar potential supported on the dual graph; this quantifies circulation and dictates corresponding 3-partitioning(s) the graph. The issue of graph embedding is revisited in Section VI where an

1

^{*}F. Ariaei and Z. Askarzadeh contributed equally as first authors. Research supported in part by the NSF under grants 1807664, 1839441, 1901599, and the AFOSR under FA9550-20-1-0029.

¹Circular propagation of action potentials known as "reentry" may lead to life-threatening conditions and sudden cardiac death [3].

example helps highlight that a given graph may have non-equivalent embeddings; these may lead to different values of macroscopic circulation. Section VII discusses potential application to cardiac circulatory abnormalities. For convenience, key notation is summarized in Table I while the Appendix highlights basic cardiac electrophysiology as background for the application in Section VII.

II. PROBABILITY FLOW FIELDS ON GRAPHS

We explain flows on graphs in the context of Markov chains. These can be thought as a canonical model to represent flows on discrete spaces in the form of probability currents induced by the Markov structure.

TABLE I: Table of notations.

Tibbb ii fuore of notations.	
Symbols	Definitions
9	directed graph $G := (\mathcal{V}, \mathcal{E})$
$\mathcal{V}, \mathcal{E}, \mathcal{F}$	node, edge, face sets
$N = \mathcal{V} $	cardinality of $\mathcal{V} = \{v_1, \dots, v_N\}; N \geqslant 3$
g_{F}	graph with adjacency-matrix zero-pattern in F
9*, 9chordal	dual and triangulated graphs
Π, π	transition probability matrix, stationary vector
$\mathfrak{d}^{\mathcal{A}}_{\mathcal{B}}$	boundary $\{(v_a, v_b) \in \mathcal{E} \mid v_a \in \mathcal{A}, v_b \in \mathcal{B}\}$
⊕ , o	entry-wise Boolean addition and multiplication
1,0	(column) vectors with all 1's and all 0's

Consider a time-homogeneous, discrete-time, N-state finite Markov chain X_t , with $t \in \mathbb{N}$, with states $\mathcal{V} = \{\nu_1, \dots, \nu_N\}$, comprised of the nodes of a network, and transition probabilities π_{ij} , i.e.,

$$\mathbb{P}\{X_{t+1} = v_i \mid X_t = v_i\} = \pi_{ii}.$$

We assume that the Markov chain is ergodic and hence, irreducible and aperiodic. Thus, the matrix $\Pi := [\pi_{ij}]_{i,j=1}^N$ has non-negative entries and is such that $\Pi \mathbb{1} = \mathbb{1}$, where $\mathbb{1}$ denotes a column vector with all entries equal to 1. The ergodicity assumption implies that for a sufficiently large integer k (e.g., k=N), Π^k has all entries positive. The dimensionality of vectors and matrices will be explicit, unless their dimension is clear from the context. The Markov chain is associated to a graph $\mathcal{G} := (\mathcal{V}, \mathcal{E})$, where the (directed) edge set \mathcal{E} is specified by the allowed transitions, i.e., $\mathcal{E} = \{(\nu_i, \nu_j) \mid \pi_{ij} \neq 0\}$. Throughout, \mathcal{G} is assumed strongly connected as it follows from the ergodicity assumption of the Markov chain.

Let now $\pi = [\pi_i]_{i=1}^N$, where $\mathbb{1}^T \pi = 1$, denote the stationary probability (column) vector of the Markov chain, i.e., $\pi^T \Pi = \pi^T$. Throughout, $(\cdot)^T$ denotes transposition and $\text{diag}(\pi_1, \dots, \pi_N) = \text{diag}(\pi)$ denotes a diagonal matrix with the specified diagonal entries. Thence,

$$P := diag(\pi_1, \dots, \pi_N)\Pi \tag{1}$$

represent probability current $p_{ij} = \pi_i \pi_{ij}$ from vertex v_i to v_i . Probability currents quantify *flux* on \mathcal{G} .

Our aim is to identify (large scale) imbalance in the *net flux* across \mathcal{G} , and to this end, we will be working mostly with the anti-symmetric part of P (modulo a factor of 1/2)

$$F = P - P^{\mathsf{T}}. (2)$$

Any element of matrix F is the difference between the incoming and outgoing flow between pairs of nodes of \mathfrak{G} , defined as $F_{ij} = p_{ij} - p_{ji}$, where p_{ij} is defined in 1. This retains information on only local flux imbalance between any two nodes, and removes all the self-loops. Note that since, $\Pi\mathbb{1} = \mathbb{1}$, it follows that $P\mathbb{1} = P^T\mathbb{1}$, and therefore, that $P\mathbb{1} = 0$ (the zero vector) as well.

Imbalance between the incoming and outgoing flow at a node indicates sink/source character which corresponds to non-vanishing divergence in the case of vector fields. Thus, we refer to a flow field F on G as "divergence free" if and only if the local net flux imbalance at every node is zero, i.e., F1 = 0. If F is not divergence free, for the purposes of this paper, it is replaced by its restriction on the complement of the range of 11^T , namely, $(I - \frac{1}{N}11^T)F(I - \frac{1}{N}11^T)$, so that F1 = 0; this is a projection onto the space of divergence-free flows.

For a flow field F on 9 originating from a Markov model, besides

$$F = -F^{T} \tag{3a}$$

$$\mathsf{F}\mathbb{1} = \mathbf{0},\tag{3b}$$

the positive part of F, namely, $F_+ := [max\{F_{ij}, 0\}]_{i,j=1}^N$, has entries that are less than or equal those in P, and since $\mathbb{1}^T P \mathbb{1} = 1$,

$$\mathbb{1}^{\mathsf{T}}\mathsf{F}_{+}\mathbb{1}\leqslant 1. \tag{3c}$$

It turns out that (3a-3c) characterize divergence-free flow fields on graphs, i.e., any antisymmetric matrix with the above properties originates from a Markovian probability structure as stated next.

Proposition 1. Consider $F \in \mathbb{R}^{N \times N}$ where (3a-3c) hold. Then F originates as a divergence-free flow-field on $G = (V, \mathcal{E})$, with |V| = N, for a Markov structure.

Proof. If (3c) holds with strict inequality, define

$$P := M + F_+, \tag{4}$$

for a symmetric matrix $M = M^T$, of the same size, with nonnegative entries such that $\mathbb{1}^T M \mathbb{1} = 1 - \mathbb{1}^T F_+ \mathbb{1}$, ensuring that $\pi^T := \mathbb{1}^T P$ has all entries positive. Now, verify that

$$\Pi = \operatorname{diag}(\pi_{\nu_1}, \dots, \pi_{\nu_N})^{-1} P \tag{5}$$

is a transition probability matrix that leads to the divergence-free flow field F. Specifically, i) Π has nonnegative entries. ii) In view of $\pi^T = \mathbb{1}^T P$ and (5), $\pi^T \Pi = \pi^T$ holds. iii) Note that $F = F_+ - F_+^T$ and hence, $F_+ \mathbb{1} = F_+^T \mathbb{1}$ from (3b). It follows that $P\mathbb{1} = P^T \mathbb{1}$, and from (5) the definition $\pi^T = \mathbb{1}^T P$, that $\Pi\mathbb{1} = \mathbb{1}$. iv) Lastly, $P - P^T = F_+ - F_+^T = F$. If (3c) holds with equality, let $P = F_+$, and define $\Pi = \text{diag}(\pi_{\nu_1}, \dots, \pi_{\nu_N})^{-1} P$. Here we have adopted the convention 0/0 = 0 in case π has zero entries. One can verify this Π is a transition probability matrix associated with the flow field F following the same arguments as before.

III. MACROSCOPIC CIRCULATION ON GRAPHS

Consider an $N \times N$ antisymmetric matrix F of net fluxes that defines a divergence-free flow field on a graph \mathcal{G} . We seek a suitable definition of (maximal) macroscopic circulation by partitioning the states into three subsets A, B, and C, in such a way so as to maximize the flux between the parts. We discuss first the simplest case, of three states, and proceed to define the concept of circulation and flow-density in general.

Three-state example: We consider a three-state Markov chain (N = 3) in Fig. 1, where for convenience we label the three nodes as A, B, C, i.e., $V = \{A, B, C\}$. The net flux matrix on G (anti-symmetric part of the probability current matrix P, modulo a factor of 1/2) is

$$F = \begin{bmatrix} 0 & -\gamma & \gamma \\ \gamma & 0 & -\gamma \\ -\gamma & \gamma & 0 \end{bmatrix},$$

with the directionality encoded in the sign of γ . Obviously, the off-diagonal entries of F must have the same magnitude, since F1 = 0. Evidently, the value $|\gamma|$ quantifies circulation in this example. The weighted oriented graph of net fluxes is shown in Fig. 2. For

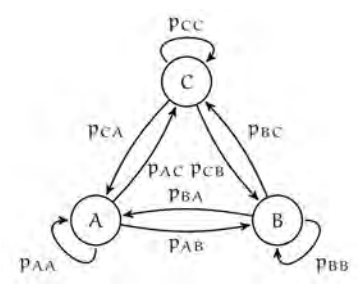


Fig. 1: Probability currents in a 3-state Markov chain.

the case of a three-state Markov chain, a close-form expression for γ can be obtained in terms of Π , though this is immaterial and not to be expected in general.

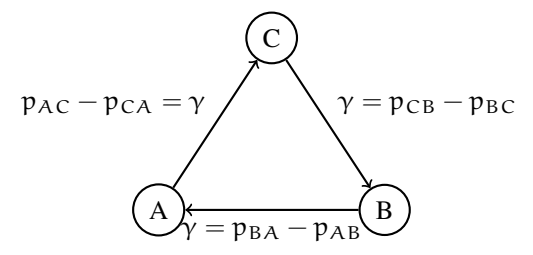


Fig. 2: Weighted oriented graph of net fluxes.

General case: We now consider the general case with N states, as before, and data for net flux between nodes in F. We seek partitioning the graph into three subsets of nodes $\mathcal{A}, \mathcal{B}, \mathcal{C} \subset \mathcal{V}$ that are pairwise non-intersecting with $\mathcal{V} = \mathcal{A} \cup \mathcal{B} \cup \mathcal{C}$.

Such a triple of subsets of V will be referred to as a 3-partition.

Define the characteristic (column) vector $I_{\mathcal{S}}$ of a set $\mathcal{S}\subseteq\mathcal{V}$, with \mathcal{V} ordered, as follows: the v^{th} entry of $I_{\mathcal{S}}$ is equal to 1 when $v\in\mathcal{S}$ and 0 otherwise. It is convenient to define entry-wise Boolean addition and multiplication of characteristic vectors, \oplus and \circ , respectively, and also the notation $\mathbb{1},\mathbf{0}$ to denote the (column) vectors with all 1's and all 0's, respectively.

Lemma 2. (A, B, C) is a 3-partition of V if and only if

$$I_{\mathcal{A}} \oplus I_{\mathcal{B}} \oplus I_{\mathcal{C}} = \mathbb{1}, \tag{6a}$$

$$I_{\mathcal{A}} \circ I_{\mathcal{B}} = I_{\mathcal{B}} \circ I_{\mathcal{C}} = I_{\mathcal{C}} \circ I_{\mathcal{A}} = \mathbf{0}, \tag{6b}$$

Proof. Relation (6a) is equivalent to $\mathcal{V} = \mathcal{A} \cup \mathcal{B} \cup \mathcal{C}$, and (6b) to pair-wise non-intersection.

Given a flow field (net-probability flux) matrix F, as before, and a 3-partition $(\mathcal{A},\mathcal{B},\mathcal{C})$ of the (ordered) vertex set \mathcal{V} , then $I_{\mathcal{A}}^TFI_{\mathcal{B}}$ is the (signed) flux directed from \mathcal{A} to \mathcal{B} . That is, if $I_{\mathcal{A}}^TFI_{\mathcal{B}} < 0$, the net flux, summed over all edges connecting directly \mathcal{A} and \mathcal{B} , is directed from \mathcal{B} into \mathcal{A} . Thus, $I_{\mathcal{A}}^TFI_{\mathcal{B}} = -I_{\mathcal{B}}^TFI_{\mathcal{A}}$, while the absolute value $|I_{\mathcal{A}}^TFI_{\mathcal{B}}|$ is the total net flux between the two parts.

Lemma 3. For any 3-partition (A, B, C) of the (ordered) vertex set V,

$$I_{\mathcal{A}}^{\mathsf{T}}\mathsf{F}I_{\mathcal{B}} = I_{\mathcal{B}}^{\mathsf{T}}\mathsf{F}I_{\mathcal{C}} = I_{\mathcal{C}}^{\mathsf{T}}\mathsf{F}I_{\mathcal{A}}.$$

Proof. Note that $I_{\mathcal{A}}^{\mathsf{T}}\mathsf{F}I_{\mathcal{A}}=0$, since F is antisymmetric, and that $I_{\mathcal{A}}\oplus I_{\mathcal{B}\cup\mathcal{C}}=I_{\mathcal{A}\cup\mathcal{B}\cup\mathcal{C}}=\mathbb{1}$. Then,

$$\begin{split} \mathbf{I}_{\mathcal{A}}^{\mathsf{T}}\mathbf{F}\mathbf{I}_{\mathcal{B}} + \mathbf{I}_{\mathcal{A}}^{\mathsf{T}}\mathbf{F}\mathbf{I}_{\mathcal{C}} &= \mathbf{I}_{\mathcal{A}}^{\mathsf{T}}\mathbf{F}\mathbf{I}_{\mathcal{B}\cup\mathcal{C}} \\ &= \mathbf{I}_{\mathcal{A}}^{\mathsf{T}}\mathbf{F}\mathbf{I}_{\mathcal{B}\cup\mathcal{C}} + \mathbf{I}_{\mathcal{A}}^{\mathsf{T}}\mathbf{F}\mathbf{I}_{\mathcal{A}} \\ &= \mathbf{I}_{\mathcal{A}}^{\mathsf{T}}\mathbf{F}\mathbf{I} = \mathbf{0}. \end{split}$$

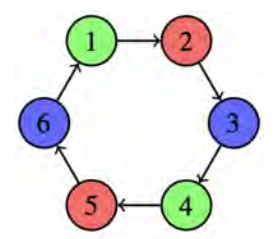


Fig. 3: 3-partition into non-contiguous pairs.

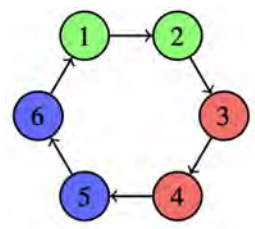


Fig. 4: 3-partition into contiguous pairs

Thus,
$$\mathbf{I}_{\mathcal{A}}^\mathsf{T}\mathsf{F}\mathbf{I}_{\mathcal{B}} = -\mathbf{I}_{\mathcal{A}}^\mathsf{T}\mathsf{F}\mathbf{I}_{\mathcal{C}} = \mathbf{I}_{\mathcal{C}}^\mathsf{T}\mathsf{F}\mathbf{I}_{\mathcal{A}}$$
. Similarly, $\mathbf{I}_{\mathcal{B}}^\mathsf{T}\mathsf{F}\mathbf{I}_{\mathcal{A}} = \mathbf{I}_{\mathcal{C}}^\mathsf{T}\mathsf{F}\mathbf{I}_{\mathcal{B}}$.

In view of the above, it is natural to define the circulation

$$c(\mathcal{A}, \mathcal{B}, \mathfrak{C}) := |I_{\mathcal{A}}^\mathsf{T} \mathsf{F} I_{\mathcal{B}}|$$

associated to any given 3-partition and, accordingly, the maximal macroscopic circulation

$$c_{max} := \max_{\text{3-partitions}} c(\mathcal{A}, \mathcal{B}, \mathcal{C}).$$

Evidently, c(A, B, C) depends on the partition as well as the "divergence-free" flow field on the graph $\mathfrak{G} = (\mathcal{V}, \mathcal{E})$ that is specified by the skew symmetric matrix F. Herein, we prefer to let F be specified from the context, instead of using a more cumbersome notation such as $c_F(A, B, C)$.

A moment's reflection reveals that these concepts do not take into account the topology of the partition. More specifically, the nature and size of the boundary between the parts of the partition may be relevant to the type of global feature we may want to capture. We highlight this point with the following example, and then return to define normalized notions of macroscopic circulation.

Six-state example: Consider hexagonal planar graph in Fig. 3 and Fig. 4. The two figures display color-coded 3-partitions, where in the first, pairs that constitute each of the three parts are not contiguous, whereas in the second, pairs of nodes in each of the three parts are neighboring and connected. The net flux matrix is

$$\mathsf{F} = \begin{bmatrix} 0 & 1 & 0 & 0 & 0 & -1 \\ -1 & 0 & 1 & 0 & 0 & 0 \\ 0 & -1 & 0 & 1 & 0 & 0 \\ 0 & 0 & -1 & 0 & 1 & 0 \\ 0 & 0 & 0 & -1 & 0 & 1 \\ 1 & 0 & 0 & 0 & -1 & 0 \end{bmatrix}.$$

Let \mathcal{A} denote the green set of nodes and \mathcal{B} the red. In the first of these two 3-partitions, $I_{\mathcal{A}}^T F I_{\mathcal{B}} = 2$, whereas in the second $I_{\mathcal{A}}^T F I_{\mathcal{B}} = 1$. The difference between the two is that the "circulatory flux" in the first 3-partition is counted *twice* due to the fact that the boundary between the parts \mathcal{A} and \mathcal{B} , denoted by $\mathfrak{d}_{\mathcal{B}}^{\mathcal{A}}$ has size 2, as it

consists of two edges, and is traversed "twice" by any complete transport around a cycle. In the second choice for a 3-partition, $\partial_{\mathcal{R}}^{\mathcal{A}} = 1$.

The above examples suggest normalizing the flux between any two parts of a partition, by dividing by the size of the corresponding boundaries. That is, normalizing $I_{\mathcal{A}}^{\mathsf{T}}FI_{\mathcal{B}}$ by dividing with the size of the boundary, namely, $|\mathfrak{d}_{\mathcal{B}}^{\mathcal{A}}|$ which denotes the cardinality of the set

$$\mathfrak{d}_{\mathfrak{B}}^{\mathcal{A}} := \{ (\nu_{\mathfrak{i}}, \nu_{\mathfrak{j}}) \mid \nu_{\mathfrak{i}} \in \mathcal{A}, \ \nu_{\mathfrak{j}} \in \mathcal{B}, \ \text{and} \ (\nu_{\mathfrak{i}}, \nu_{\mathfrak{j}}) \in \mathcal{E} \}$$

of edges between the two parts A, B, brings us to a notion of *density flux* associated with the boundary separating two parts of any partition,

$$f(\mathfrak{d}^{\mathcal{A}}_{\mathcal{B}}) := \frac{|I^{\mathsf{T}}_{\mathcal{A}}FI_{\mathcal{B}}|}{|\mathfrak{d}^{\mathcal{A}}_{\mathcal{B}}|}.$$

Accordingly, the minimal density flux of the partition, is

$$f_{\min}(\mathcal{A}, \mathcal{B}, \mathcal{C}) := \min\{f(\partial_{\mathcal{B}}^{\mathcal{A}}), f(\partial_{\mathcal{C}}^{\mathcal{B}}), f(\partial_{\mathcal{A}}^{\mathcal{C}})\}, \quad (7)$$

and similarly for the maximal. This approach leads us to a combinatorial problem. In fact, for a graph with n vertices, the total number of possible cases to consider for solving (7) is equal to Stirling number of the second kind, S(n,3) [15]. Thus, below, we focus on planar graphs and explain how to compute suitable notions of macroscopic circulation via a scalar potential supported on the dual graph.

IV. PLANAR GRAPHS AND NETWORK CIRCULATION

We assume that geographic proximity of nodes is dictated by an actual embedding of a graph into a linear metric space, specifically \mathbb{R}^2 . Graphs that can be embedded in \mathbb{R}^2 , without intersection of edges, are called *planar*. In this case flow fields have a strong resemblance to planar vector fields.

For planar vector fields there is a well known decomposition into gradient flow and curl that captures circulation. In fact, circulation can be conveniently quantified by a scalar potential. In a similar manner, for planar graphs, circulation relates to a scalar potential on the vertex set of a dual graph as we will explain shortly. The dual \mathcal{G}^* of a planar graph \mathcal{G} is itself a planar graph whose vertices correspond to faces of \mathcal{G} , and whose faces correspond to vertices of \mathcal{G} . Nodes in \mathcal{G}^* are connected by an edge if the corresponding faces in \mathcal{G} have an edge as boundary. We proceed to review some facts on planar graphs, as well as elements of the Helmholtz-Hodge decomposition of vector fields that provides insight into the corresponding decomposition of flow fields on graphs.

A. Planar graphs

A graph is referred to as *planar* when it can be drawn on the plane in a way that no edges cross each other and intersect only at their endpoints (vertices). The study of planar graphs goes back to Euler who showed that, for simple and connected planar graphs on the simply connected space \mathbb{R}^2 , i.e., with zero genus q,

$$|\mathcal{V}| - |\mathcal{E}| + |\mathcal{F}| = \chi(\mathfrak{g}) = 2 \tag{8}$$

where \mathcal{F} is the set of faces² and the Euler characteristic³ is $\chi(g) = 2 - 2g$. Euler's formula is not sufficient to ensure planarity. A condition that fully characterizes planarity was given in 1930's by Kuratowski and Wagner in the form of absence of two specific subgraphs, K_5 or $K_{3,3}$ [16].

The next important consideration is how to embed a planar graph in \mathbb{R}^2 . For this we refer to [17]. It turns out that there may exist several "nonequivalent embeddings" [18], [19]. As we explain below, network circulation depends on the particular embedding.

Every planar graph can be drawn on a sphere (and vice versa) via stereographic projection. This amounts to identifying points on \mathbb{R}^2 with points on the (Riemann) sphere by corresponding the "north pole" with the "point at ∞ " and any other pair in line with the north pole (the line containing a point on the sphere and the corresponding projection on \mathbb{R}^2) (see Fig. 5).

For any planar graph \mathcal{G} , and any face f of \mathcal{G} , the graph can be redrawn on the plane in such a way that f is the "outside face" of \mathcal{G} . This can be effected by rotating the projection of the graph onto the Riemann sphere so that the image of the face contains the north pole. However, besides slid-

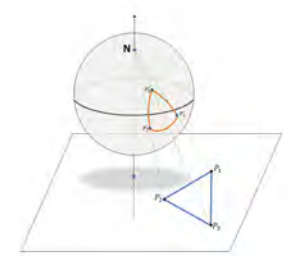


Fig. 5: Stereographic projection.

ing and rotating the graph projection on the Riemann sphere, other transformations are possible that may change the local ordering of vertices, leading to non-equivalent embeddings of the graph on \mathbb{R}^2 .

More precisely, for our purposes, two graph embeddings are said to be *equivalent* if their corresponding

projections onto the sphere can be continuously rotated (and the corresponding vertices shifted onto the sphere without crossing edges) so as to match. The equivalence of two graphs is exemplified in Fig. 6. For the reasons we just explained, that the positioning of the north pole leads to equivalent embeddings, there are $|\mathcal{F}|$ isomorphic embeddings for every planar graph, as stated next.

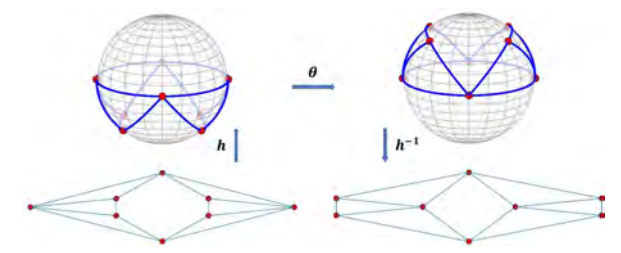


Fig. 6: Isomorphic graphs and sequence of graph morphisms; θ and h are rotation and projection maps, respectively.

Lemma 4. There are $|\mathfrak{F}|$ isomorphic embeddings for every planar graph.

Proof. Fig. 6 exemplifies the equivalence between two planar embeddings, as discussed leading into the lemma. More specifically, consider a graph \mathcal{G} with a given embedding $h: \mathbb{R}^2 \to S^2$ that maps \mathcal{G} to \mathcal{G}_s on sphere S^2 . A homeomorphism $\theta: S^2 \to S^2$ rotates the position of nodes and edges of \mathcal{G}_s on the outside of S^2 , placing the "north pole" within any of the $|\mathcal{F}|$ possible faces. Then, $h^{-1} \circ \theta \circ h$ produces an equivalent graph embedding. \square

B. Helmholtz-Hodge decomposition

We now turn to a brief overview of concepts of vector fields. The Helmholtz-Hodge decomposition simplifies the analysis by bringing up important properties such as incompressibility and vorticity that can thereby be studied directly [20].

The Helmholtz-Hodge decomposition states that the space of vector fields decomposes into mutually L^2 -orthogonal sub-spaces using potential functions [21]. The components can be calculated as the gradient of a scalar potential φ and curl of a vector potential ψ , namely,

$$W = \nabla \Phi + \nabla \times \Psi + h,$$

where $\nabla \phi$ is the curl-free component (i.e., $\nabla \times \nabla \phi = 0$) of the vector field \mathcal{W} , and $\nabla \times \psi$ is its divergence-free component (i.e., $\nabla \cdot \nabla \times \psi = 0$), whereas the harmonic component h is both divergence-free and curl-free.

The curl-free component: Since the divergence of a curl is zero, we can compute ϕ , the scalar potential associated

²The exterior of the graph needs to be counted as a face, and it is referred to as the outside face.

³Euler characteristic is a topological invariant, a number that describes a topological space's shape regardless of the way it is "bent."

with the curl-free component of the vector field W, as the solution of the following Poisson equation.

$$\nabla \cdot \mathcal{W} = \nabla \cdot \nabla \Phi = \nabla^2 \Phi$$

where the last equality holds because the divergence of a gradient is the Laplacian.

The divergence-free component: Since the vorticity (normal component of the surface curl) of a gradient field vanishes, $\hat{\mathbf{n}}$. $(\nabla \times \mathcal{W}) = \hat{\mathbf{n}}$. $(\nabla \times \psi)$. Since vorticity of the surface curl of a scalar potential is the surface Laplacian of the potential, we have

$$\hat{\mathbf{n}} \cdot (\nabla \times \mathcal{W}) = \Delta \psi \tag{9}$$

where $\hat{\mathbf{n}}$ is the normal vector. Equation (9) is obeyed if the scalar field ψ is a solution of the above Poisson equation.

In the case of vector fields on \mathbb{R}^2 , the curl can be expressed as $\Psi = J\nabla \psi$, where J is an antisymmetric matrix and ψ a scalar potential. It follows (Stokes' theorem) that the flux crossing any curve connecting two points α and b on \mathbb{R}^2 is given by the difference of the endpoint potentials, hence, we have the following.

Proposition 5. The flux across the path connecting the extrema of a curl potential field is maximum.

Proof. With J the operator that rotates a vector on \mathbb{R}^2 counter-clockwise by 90°, the flux between a and b is

$$I_{ab} = \int_{a}^{b} J\nabla\psi \cdot Jds = \psi(b) - \psi(a), \qquad (10)$$

and

$$max(I_{\alpha b}) = \max_{\alpha, b \in \mathbb{R}^2} (\psi(b) - \psi(\alpha)). \tag{11}$$

An analogue of Proposition 5 over discrete vector fields on graphs is discussed next.

C. Planar Net Flux Graph

Starting with an antisymmetric net flux matrix $F = [F_{ij}]_{i,j}$ in (2) of a Markov chain on a planar graph, we consider the graph with adjacency matrix having the zero pattern of F; the space of vertices and edges are the collection of the nodes and edges, respectively, that have corresponding non-zero elements in F, $\mathcal{V}_F = \{v_i \in \mathcal{V}|F_{ij} \neq 0$ for some $v_j \in \mathcal{V}\}$, $\mathcal{E}_F = \{e_{ij} \in \mathcal{E} \mid F_{ij} \neq 0\}$. In addition we specify a sign function $\sigma: \mathcal{V}_F \times \mathcal{V}_F \to \{-1,1\}$ that assigns an orientation, specifically $\sigma(i,j) = \text{sign}(F_{ij})$ for all non-zero elements of the net flux matrix, and define the directed graph $\mathcal{G}_F(\mathcal{V}_F, \mathcal{E}_F, \sigma)$. This is a simple graph in that at most one edge exists between pairs of nodes. The vector of edge flow weights

$$\mathcal{W} = (w_{ij})_{i,j}$$

corresponding to edges $e_{ij} \in \mathcal{E}_F$ with values $w_{ij} = |F_{ij}|$ represents the flow field. The space of all flow fields is denoted by \mathcal{U}_F and assumes a Helmholtz-Hodge decomposition,

$$\mathcal{U}_{\mathsf{F}} = \mathcal{U}_{\mathsf{F}}^{\mathsf{curl}} \oplus \mathcal{U}_{\mathsf{F}}^{\mathsf{harmonic}} \ \oplus \mathcal{U}_{\mathsf{F}}^{\mathsf{gradient}},$$

where $\mathcal{U}_F^{gradient}$ and \mathcal{U}_F^{curl} are curl-free and divergent-free components and \oplus denotes the direct sum of vector spaces. If \mathcal{W}_{curl} , $\mathcal{W}_{harmonic}$, $\mathcal{W}_{gradient}$ denote projections of \mathcal{W} in the respective components, then clearly $\mathcal{W}_{gradient} = \mathbf{0}$, since by assumption F has no "sources."

We wish to capture circulation in a similar manner as in planar flow fields and thereby we seek a curl potential ψ . The harmonic component $\mathcal{W}_{harmonic}$ relates to circulation about "holes" (non-triangular faces [13]) in the graph. Thus, before we proceed, we triangulate \mathcal{G}_F , and generate a new graph $\mathcal{G}_F^{chordal}$ so as to remove holes and ensure that the harmonic component is zero.

D. Triangulated Planar Graph

The curl component of the flow field is defined on triangles, i.e., cycles of length 3 [13]. The cycle graphs of more than 3 vertices are considered as holes and their edge flow as harmonic components of the flow field.

To remove the harmonics, we replace the holes that are not bounded by triangles with chordal subgraphs. That is, we add a minimum number of chords, as edges with zero flux, that are not part of the cycle but each connects two vertices of the cycle. This way, we generate a planar chordal graph such that every chordless cycle subgraph is a triangle. Fig. 10 in Section VI shows examples of triangulated graphs with the original graphs in Fig. 9). It turns out that graph triangulation strongly depends on the embedding, which will be again discussed in Section VI. The corresponding potential function ψ is defined on the graph's faces, and hence, can be assigned to the nodes of the dual graph, $(\mathcal{G}_{\mathsf{F}}^{\mathsf{chordal}})^*$. The potential ψ takes the same value on each triangular face that originates in the same original non-triangular face. The maximum flux, in complete analogy with (11), is then obtained by identifying those vertices of the dual graph with minimum and maximum curl potentials.

E. Non-planar Graphs

Graphs that cannot be drawn on a plane or sphere without edge crossings, i.e., non-planar, can always be drawn on a surface of higher genus [22]. A surface is said to be of genus $g \in \{0, 1, 2...\}$ if it is topologically

homeomorphic to a sphere with g handles. For instance, the genus of a sphere is 0, and that of a torus is 1. Accordingly, a graph is said to have genus g if it can be drawn without crossings on a surface of genus g, but not on one of genus g - 1. It can be easily seen that K_5 and $K_{3,3}$ are graphs of genus 1 (toroidal graphs); Fig. 7 exemplifies $K_{3,3}$ drawn on the torus T^2 . The graph is drawn by assigning points and continuous, nonintersecting (except at end-points) paths corresponding to the vertices and edges of the graph, respectively. The dual of a non-planar graph can also be drawn on the torus in a similar fashion to a planar graph.

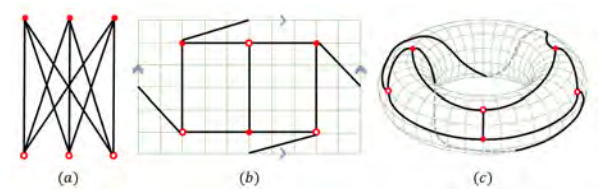


Fig. 7: A toroidal graph $(K_{3,3})$: (a) Embedding on \mathbb{R}^2 ; (b) The projective plane; (c) Embedding on a torus.

The decomposition of a continuous vector field on the torus (as a manifold) is more complicated than on a sphere. In this case, the divergence-free component $\mathcal{U}_F^{\text{curl}}$, can be partitioned into a toroidal and a poloidal part [23], [24] –a restricted form of the usual Helmholtz decomposition. We contend that an analogous decomposition of a flow field of genus 1 graph can be similarly obtained; the corresponding poloidal component is once again generated by a scalar potential (as in the case of planar graphs) whereas the poloidal component is harmonic and represents flux/circulation around holes (of the torus). A detailed analysis on how to compute maximal graph circulation for graphs of genus 1 is not available at present.

V. GRAPH PARTITIONING

We summarize the insights gained and highlight the steps needed in Algorithm 1 which helps obtain a 3-partition corresponding to maximal circulation by providing the curl potential ψ on the vertices of its dual graph (i.e., faces of the original graph) and how to numerically calculate these. The outcome depends on the embedding of \mathcal{G}_F (cf. Section VI).

Knowing ψ allows carving 3-partitions that entail maximal circulation. Indeed, any set of two paths on the dual graph between the points of ψ -extrema separates the graph in the three regions, A, B and C, discussed earlier. This is summarized next.

Theorem 6. Consider a divergence-free flow field W on the edges of a strongly connected directed graph.

Algorithm 1: Finding curl potential extrema

Input:

An embedded strongly connected, aperiodic, planar graph G with transition matrix Π .

Offline Preprocessing:

- 1. Calculate the net flux matrix F from (2).
- 2. Construct and triangulate \mathcal{G}_F as described in Section IV-C, to generate $\mathcal{G}_F^{chordal}$.
- 3. Find dual graph (\$\mathcal{G}_F^{chordal}\$)*.
- 4. Set the potential ψ for the outside face to zero.

Computations:

Find potential ψ for vertices of the dual graph using (10), i.e., obtain ψ so that the difference between values at the nodes of the dual graph (corresponding to faces of the primal) equals the flux of the corresponding edge of the primal graph, $\psi(\text{face}_{\text{left}}) - \psi(\text{face}_{\text{right}}) = F_{ij}$ assuming a consistent orientation.

Output:

Two faces of the primal with potential extrema.

Algorithm 1 generates the chordal directed graph $\mathcal{G}_F^{chordal}$ and its dual with an associated curl potential ψ . There exist paths in the dual graph connecting two chosen extrema points of ψ that provide a 3-partition with maximal macroscopic circulation.

Proof. Completion of the graph into a chordal graph is the first step of the algorithm and was explained before. We compute ψ as follows. We assign 0 at the vertex of the dual of the chordal graph corresponding to the outside face, and proceed to assign values to the remaining vertices of the dual graph so that the difference between values of adjacent vertices equals the (signed, e.g., in the counter-clockwise sense) flux on the corresponding edge of the primal graph. We now explain the last part of the theorem.

Since $\mathcal{G}_{\mathsf{F}}^{\mathsf{chordal}}$ is triangulated, its dual is 3-edge-connected [25]. By Menger theorem [26], for 3-edge-connected graphs every pair of vertices has 3 edge-disjoint paths in between. Now consider a pair of vertices on the dual graph, ν_{\min}^* and ν_{\max}^* , corresponding to the minimum and maximum of ψ , respectively. There are 3 edge-disjoint paths P_1 , P_2 , and P_3 , connecting ν_{\min}^* and ν_{\max}^* . These paths can generate three cycles as follows.

$$C_{ij} = P_i \cup P_j$$
, $(1 \leqslant i < j \leqslant 3)$

where $C_{ij} \in \mathcal{C}$, and \mathcal{C} is a family of cycles in $(\mathcal{G}_F^{\text{chordal}})^*$.

If paths P_1 , P_2 , and P_3 are also internally disjoint, then they will generate three cycles C_{12} , C_{23} , and C_{13} . If C_{12}

and C_{23} are contractible, by 3-path condition [27]–[29], C_{13} is also contractible. We only need to show that if P_2 lies between P_1 and P_3 , then C_{13} is surface separating and⁴ $\operatorname{int}(C_{13}) = \operatorname{int}(C_{23}) \cup \operatorname{int}(C_{12}) \cup P_2$. It follows from Euler's formula that the genus of $\operatorname{int}(C_{13}) \cup C_{13}$ is zero, and thus C_{13} is contractible.

Since C_{ij} 's are also discrete Jordan curves and equivalent to the bonds of $\mathcal{G}_F^{chordal}$ [22], [30], by properly selecting interior or exterior of those cycles, these delineate three disjoint and connected sets of primal vertices. Then, by (11), the flow that crosses their shared boundaries (i.e., P_1 , P_2 , and P_3) is maximal.

If P_1, P_2, P_3 are edge-disjoint paths between v_{\min}^* and v_{\max}^* , but not internally disjoint, there exists cycles C_{ij} 's that are self-intersecting. That is, the $\operatorname{int}(C_{ij})$ is not path-connected and, hence, not contractible.

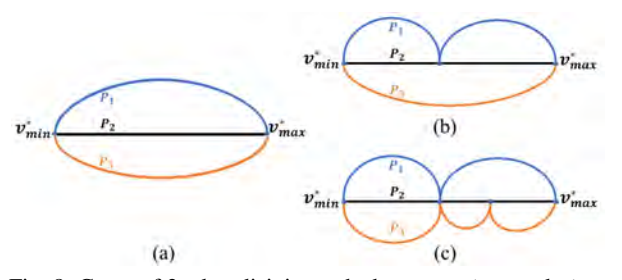


Fig. 8: Cases of 3 edge-disjoint paths between v_{\min}^* and v_{\max}^* : P_1, P_2, P_3 are (a) internally disjoint, (b,c) not internally disjoint.

Fig. 8 exemplifies cases discussed in the above proof. In case (a) the three cycles $C_{12} = P_1 \cup P_2$, $C_{23} = P_2 \cup P_3$, and $C_{13} = P_1 \cup P_3$ are contractible. Therefore, all 3-partitions, $\operatorname{int}(C_{12}), \operatorname{int}(C_{23}), \operatorname{ext}(C_{13})$ are connected. The cases (b,c) correspond to cycles that are self-intersecting. Specifically, in Fig. 8(b) only C_{12} is self-intersecting, whereas in Fig. 8(c) all three cycles are self-intersecting. Accordingly, the corresponding 3-partitions may not be connected.

Corollary 7. *If there exist 3 edge-disjoint paths that are vertex-disjoint, then each 3-partition is connected.*

Fig. 10 exemplifies Theorem 6 for a planar graph with two non-equivalent embeddings, where P_1, P_2, P_3 are marked with different colors and the 3-partitions are marked using different colors (red, blue, green) and shapes $(\Box, \bigcirc, \triangle)$. In the next section we explain how the output of Algorithm 1, and consequently the partitioning, depends on the embedding.

VI. EFFECT OF EMBEDDING

It is known that 3-connected graphs have unique embedding, and consequently a unique dual graph [18]. But in general, different embeddings with non-isomorphic duals are possible. This is of importance since the output of Algorithm 1 depends on the dual graph. We highlight the issue with an example.

Fig. 9 displays two non-isomorphic embeddings of the same graph. Assuming a transition probability matrix

$$\Pi = \begin{bmatrix}
0 & 0.25 & 0 & 0 & 0.25 & 0 & 0.25 & 0.25 \\
0.333 & 0 & 0.333 & 0.333 & 0 & 0 & 0 & 0 & 0 \\
0 & 0.25 & 0 & 0.25 & 0 & 0.25 & 0 & 0.25 \\
0 & 0.333 & 0.333 & 0 & 0.333 & 0 & 0 & 0 & 0 \\
0.333 & 0.333 & 0 & 0.333 & 0 & 0 & 0 & 0 & 0 \\
0 & 0 & 0.333 & 0 & 0 & 0 & 0.333 & 0.333 \\
0.5 & 0 & 0 & 0 & 0 & 0.5 & 0 & 0 & 0 \\
0.25 & 0 & 0.25 & 0 & 0 & 0.25 & 0.25 & 0
\end{bmatrix},$$
(12)

we apply Algorithm 1 to obtain the net flux matrix, triangulated graphs, and the respective 3-partitions shown in Fig. 10. The maximal circulation is 0.0301 and 0.0321, and the corresponding 3-partitions are $\{\{7\}, \{8\}, \{1, 2, 3, 4, 5, 6\}\}$ and $\{\{4, 8\}, \{2, 3, 6\}, \{1, 5, 7\}\}$, respectively.

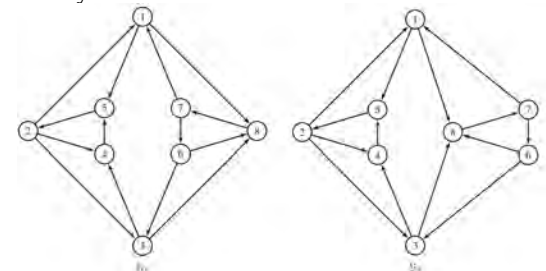


Fig. 9: Non-equivalent embeddings of the same graph.

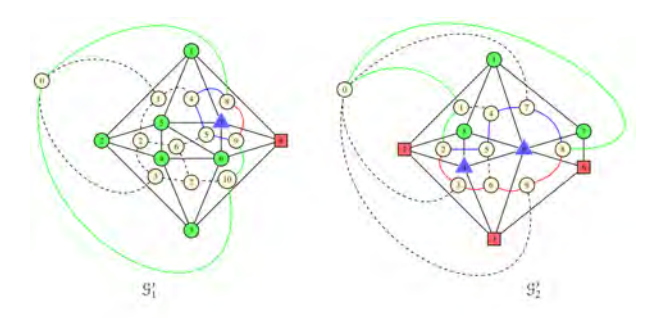


Fig. 10: Triangles, duals and 3-partitions of graphs in Fig. 9.

VII. APPLICATION TO CARDIAC CIRCULATION

We now discuss the potential relevance of network circulation for detecting and quantifying a specific pathology that relates to what is known as "reentry" in cardiac conduction systems. It is noted that application of graph theory to cardiac electrophysiology is fairly new [31].

 $^{^{4}}$ int(·) and ext(·) denote interior and exterior, respectively.

A. Background

Reentry refers to a pathologic impulse conduction that underlies a self-sustaining cardiac rhythm abnormality. This may account for most tachyarrhythmias found in patients that lead to life-threatening arrhythmias and sudden cardiac death [3]. A model for reentry is shown in Fig. 11(a). In normal conduction, a single action potential [32] travels down each branch and through a common, connecting pathway across the "active medium" that constitutes the heart muscle. In reentry, the action potential propagates in a circus-like closed-loop manner, continuously depolarizing the cardiac muscles around an abnormal area. It can take place within a small local

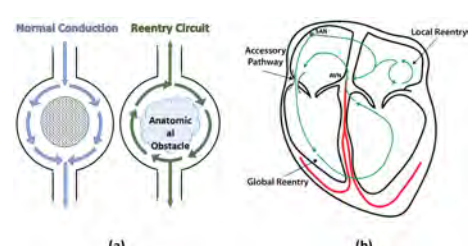


Fig. 11: (a) Normal conduction and reentry circuit; (b) Local and global reentry in heart.

region within the heart or it can occur between the atria and ventricles (global reentry) (see Fig. 11(b)), and can cause atria and/or ventricular tachycardia. Local reentry could be the result of conduction blocks, whereas global reentry is formed due to accessory pathways (muscle bridges, known as Kent bundles). A well-known complication is the Wolff-Parkinson-White (WPW) pattern that can transition into ventricular tachycardia and sudden death without prompt diagnosis and treatment [3]. A permanent treatment is *cardiac ablation* that destroys the abnormal conduction pathways with heat. To avoid complications it is crucial to locate the abnormal conduction pathways by precise cardiac mapping [33].

B. Method

A model of the heart conduction system as a directed graph, with nodes representing cardiac cells, can help locate local or global re-entrant circulation. Cardiac cells can be grouped as specialized cells that have automatic action potential generation capability (Sinoatrial (SA) node, Atrioventricular (AV) node, and Purkinje fibers) that can be viewed as sources, and excitable cells and fiber membranes. It should be noted that all cardiac cells may have sink-source properties⁵

[34]. A simplified illustration of a directed graph model of heart is shown in Fig. 12. For simplicity, only a few nodes are depicted and the directed arrows show a time frame of the current propagation patterns. A 3-partition is also highlighted by sets of nodes in green circles, red squares, and blue triangles. Fig. 12 also illustrates the atrioventricular circulation of excitation (global reentry) WPW pattern (yellow arrow).

The following example is based on a standard 12-lead surface electrocardiogram (ECG) of a WPW pattern presented in [35] and displayed in Fig. 18 in the Appendix. The voltage (electric potential) in mV was read from the patient's ECG for each of the 12



Fig. 12: An illustration of directed graph modeling of heart, global reentry, and 3-partitions.

"physical" leads and transformed to XYZ "virtual" leads (xyz-coordinates on a sphere with the origin at the center of the heart) via

$$\Phi_{t} = T V_{t} \tag{13}$$

where $V_t \in \mathbb{R}^{12}$ is the vector of the 12 leads' voltages, $\Phi_t = (V_X, V_Y, V_Z)^T \in \mathbb{R}^3$ is the vector of the XYZ leads' potentials, T is a transformation matrix⁶, while t denotes time. The vector potential, Φ_t , (also known as vector ECG) measures of cardiac electrical activities; its magnitude is shown in Fig. 13. For the purposes of our analysis we sampled $\Phi_t \in \mathbb{R}^3$ every 0.2sec over the interval of [0.8sec, 2.4sec] highlighted in the figure.

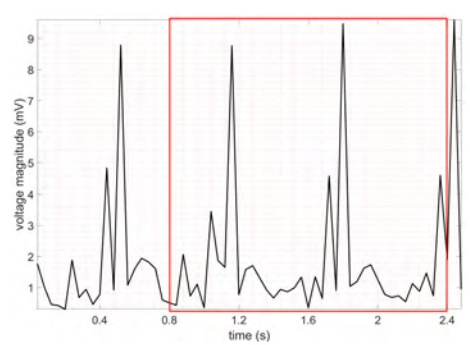


Fig. 13: Magnitude of vector ECG; the red rectangle boxes the computational time-frame.

We form a graph on the sphere with "virtual" nodes at 9 locations in the direction of each vector in $\{\Phi_{0.8}, \Phi_1, \dots, \Phi_{2.4}\}$. This is shown in Fig. 14 along

⁵During action potential propagation, an excited cell serves as a source, whereas during the absolute refractory period it serves as a sink [32].

⁶Analogous transformations to transform 12-lead ECG signals to 3-lead vector ECG and vice versa can be found in [36], [37].

with the stereographic projection onto a planar graph. This vertex set represents collection of heart's excitable cells that are excited at various instances in time. A potential equal to the corresponding magnitude of the vector ECG is associated with each vertex. We set $\varphi = (\|\Phi_{0.8}\|, \|\Phi_1\|, \dots, \|\Phi_{2.4}\|)^T \in \mathbb{R}^9.$

Edges are specified when an estimated net-current between pairs of nodes is above a threshold. Specifically, from the vector ϕ of electric potentials we compute potential differences $\delta \phi_{ij} = \phi_i - \phi_j$, for all pairs of vertices, and using Kirchhoff's and Ohm's laws we calculate the (virtual) flow $y_{ij} = R_{ij}^{-1} \delta \phi_{ij}$ on potential edges [38], [39]; $R_{(ij)} = \rho L_{(ij)}/area$ where area is the cross section of heart muscles, assumed to be unity, and $L_{(ii)}$ is the physical distance between nodes on the heart. (Physical distance on the heart between nodes can be computed by the timing of traveling action potentials.) For simplicity we assume that the electrical resistivity of cardiac muscle is $\rho = 268 \; (\Omega.cm) \; [40]$. The divergence free net flux matrix F (i.e, the net-current between nodes) is generated from y. By Algorithm 1, we calculate the curl potentials on the dual graph, and the corresponding 3-partitions explained earlier.

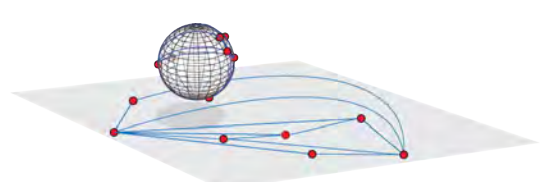


Fig. 14: Stereographic projection of vector ECG.

C. Discussion

figure

The time window on the 12-lead ECG was chosen to capture propagation of action potentials through the heart muscles in at least one cycle. The maximum and minimum curl potentials were found that led to the 3-partition {{5},{6},{1,2,3,4,7}} shown in Fig. 15. The

highlights

planar directed graph of

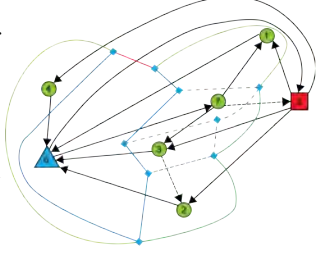


Fig. 15: Triangulated graph of vector ECG and 3-partitions.

divergence free flow and the corresponding 3-parts with red squares/blue triangles/green circles, respectively. Isolated nodes are omitted for simplicity. The figure shows that the flow is supported mostly by paths through groups of cardiac cells in the patient's right atrium and ventricle, interpreting the readings from the ECG in

the

Fig. 18. It also underscores the path between nodes 6 and 5 (edge (5,6)) that could be a candidate point for ablation. Whereas the results of our analysis are not be entirely conclusive, they may provide guidance to physicians and a basis for potentially powerful future diagnostic tools.

VIII. CONCLUDING THOUGHTS

We have introduced maximal graph circulation of divergence free flows on graphs and their connection to suitable 3-partitions. The 3-partitions can be seen as "communities" (of nodes, cells, etc.) on the path that supports a maximizing circulatory current. Whereas computational issues for general graphs remain a combinatorial challenge, planar graphs are amenable to a rigorous analysis framework.

A motivating application for our work originates in cardiac electrophysiology. Because the heart muscle is homeomorphic to a sphere, analysis of propagating currents and action potentials to identify circulation is possible using the proposed framework. To this end, we worked out a suggestive example. However, the conclusions are tentative as a more detailed analysis and reliable data set are warranted. In this context, it is our hope that the concepts laid out will facilitate the development of diagnostic tools for detecting the source of arrhythmias and potential target cells for ablation.

APPENDIX: ON CARDIAC ELECTROPHYSIOLOGY

We now provide background for the application in Section VII. For a more complete expository on the topic see [32], [41], [42].

The heart is an organ at the center of the human's circulatory system that pumps blood through the body. It is made up of multiple layers of tissue, such as specialized excitatory and conductive muscle fibers that exhibit either automatic rhythmical electrical discharge in the form of action potentials or conduction of the action potentials through the heart. Action potential is electrical stimulation created by a sequence of ion fluxes through specialized channels in the membrane of cardiomyocytes that leads to cardiac contraction.

The heart's electrical conduction system controls the rate and rhythm of the heartbeat. A group of the specialized cells is located in the superior posterolateral wall of the right atrium, known as *sinoatrial* (SA) node. The SA node depolarizations are transmitted to both the antrioventricular (AV) node and the Purkinje fibers

and discharge both before their own threshold for selfexcitation can occur. SA node virtually serves as the pacemaker of the normal heart.

The recording of the electrical voltages from the surface of the heart is known as an electrocardiogram (ECG). A normal ECG is composed of a P wave, a QRS complex and a T wave. Both the P wave and QRS complex are depolarization waves and the T wave is the re-polarization wave (see Fig. 16). Abnormalities in the shape and duration of the ECG waveform is an indication of underlying heart conditions.

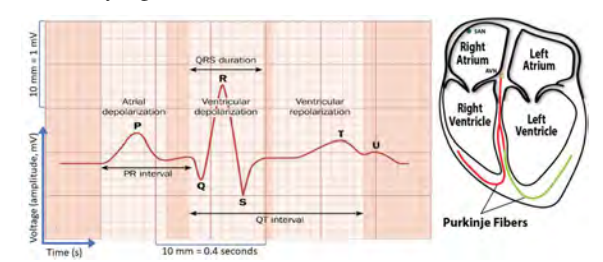


Fig. 16: The normal ECG waveform.

The most common type of ECG machines include 12 leads which can be used to capture the multi-directional view of space-time cardiac electrical activities from twelve different angles. Fig. 17 shows the position of the leads. Lead I, II, and III are the three bipolar leads, recording the voltage differences of elec-

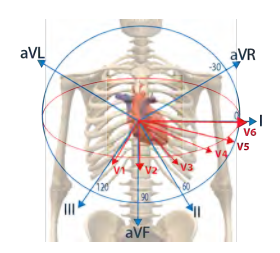


Fig. 17: The 12-lead ECG positioning (body coordinate system).

trodes placed on the limbs. They observe the heart from an angle of 0° , 60° , and 120° , respectively. Leads V1 to V6 are six chest leads, recording the voltage differences of electrodes placed directly over the heart and an indifferent electrode which is connected to the right and left arms and left leg at the same time. Leads aVL, aVR and aVF are augmented unipolar limb leads and looking at the heart from an angle of -30° , -150° , and 90° , respectively. The example of 12-lead surface ECG of a patient with WPW pattern used in our analysis in Section VII is shown in Fig. 18.

REFERENCES

- S. Zahid et al., "Feasibility of using patient-specific models and the "minimum cut" algorithm to predict optimal ablation targets for left atrial flutter," Heart Rhythm, vol. 13, no. 8, pp. 1687– 1698. 2016.
- [2] M. Constantinescu, S.-L. Lee, S. Ernst, and G.-Z. Yang, "Traversed graph representation for sparse encoding of macroreentrant tachycardia," in *Statistical Atlases and Computational Models of the Heart*. Springer, 2015, pp. 40–50.

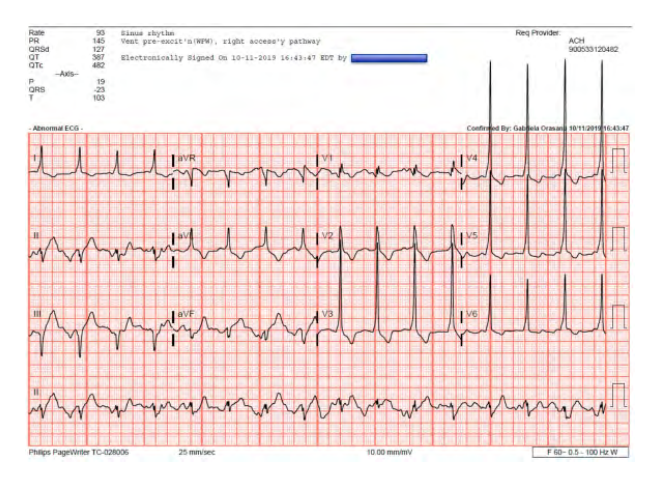


Fig. 18: 12-lead ECG recording of a patient with WPW pattern from [35]: the resolution is 2 squares/mV (vertically) vs. 5 squares/sec (horizontally).

- [3] A. Goyal, P. Senst, B. Bhyan, and R. Zeltser. (2020, September) Reentry arrhythmia. [Online]. Available: https://www.ncbi.nlm.nih.gov/books/NBK537089/
- [4] C.-E. Bichot and P. Siarry, Graph partitioning. Wiley Online Library, 2011.
- [5] O. Mason and M. Verwoerd, "Graph theory and networks in biology," *IET systems biology*, vol. 1, no. 2, pp. 89–119, 2007.
- [6] G. Pavlopoulos, M. Secrier, and C. Moschopoulos, "Using graph theory to analyze biological networks," *BioData Mining*, vol. 4, no. 10, 2011.
- [7] R. Andersen, F. Chung, and K. Lang, "Using pagerank to locally partition a graph," *Internet Math.*, vol. 4, no. 1, pp. 35–64, 2007.
- [8] ____, "Local partitioning for directed graphs using pagerank," Internet Math., vol. 5, no. 1-2, pp. 3–22, 2008.
- [9] D. Wang, W. Chen, and L. Qiu, "Multi-leader selection in complex networks," in 2016 IEEE 55th Conference on Decision and Control (CDC). IEEE, 2016, pp. 1751–1756.
- [10] S. Arora, S. Rao, and U. Vazirani, "Expander flows, geometric embeddings and graph partitioning," *Journal of the ACM (JACM)*, vol. 56, no. 2, p. 5, 2009.
- [11] Fan Chung, "Laplacians and the Cheeger inequality for directed graphs," *Annals of Combinatorics*, vol. 9, no. 1, pp. 1–19, 2005.
- [12] A. Muhammad and M. Egerstedt, "Control using higher order laplacians in network topologies," in *Proc. of 17th International Symposium on Mathematical Theory of Networks and Systems*, *Kyoto*, 2006, pp. 1024–1038.
- [13] L. Lim, "Hodge Laplacians on graphs," SIAM Rev., vol. 62, p. 685–715, 2019.
- [14] A. Muhammad, R. Ghrist, and M. Egerstedt, "Beyond graphs: higher dimensional structures for networked control systems," to appear, Control Sys, 2006.
- [15] J. Quaintance, Combinatorial Identities for Stirling Numbers: The Unpublished Notes of H W Gould. World Scientific, 2015.
- [16] C. Thomassen, "Planarity and duality of finite and infinite graphs," *Journal of Combinatorial Theory, Series B*, vol. 29, no. 2, pp. 244–271, 1980.
- [17] G. Nemhauser and L. Wolsey, "Integer programming and combinatorial optimization," in Wiley, 1988. Springer, 1999.
- [18] H. Whitney, "Congruent graphs and the connectivity of graphs," in H. Whitney Collected Papers. Springer, 1992, pp. 61–79.

- [19] A. Gagarin, W. Kocay, and D. Neilson, "Embeddings of small graphs on the torus," *Cubo Mat. Edu.*, vol. 5, 2003.
- [20] W. V. D. Hodge, The theory and applications of harmonic integrals. Cambridge University Press, 1941.
- [21] H. Bhatia et al., "The Helmholtz-Hodge decomposition-a survey," IEEE Transactions on Visualization and Computer Graphics, vol. 19, no. 8, pp. 1386–1404, 2012.
- [22] R. J. Wilson, Introduction to graph theory. Pearson Education India, 1979.
- [23] F. Razafindrazaka et al., "Hodge decomposition of wall shear stress vector fields characterizing biological flows," Royal Society Open Science, vol. 6, 2019.
- [24] M. Berger and G. Hornig, "A generalized poloidal-toroidal decomposition and an absolute measure of helicity," *Journal of Physics A: Mathematical and Theoretical*, vol. 51, no. 49, 2018.
- [25] J. L. Gross and J. Yellen, Handbook of graph theory. CRO press, 2003.
- [26] C. Doczkal, "Short proof of Menger's theorem in coq (proof pearl)," *HAL-02086931*, 2019.
- [27] C. Thomassen, "Embeddings of graphs with no short noncontractible cycles," *Journal of Combinatorial Theory, Series B*, vol. 48, no. 2, pp. 155–177, 1990.
- [28] B. Mohar and C. Thomassen, *Graphs on surfaces*. Johns Hopkins University Press Baltimore, 2001, vol. 16.
- [29] É. C. De Verdière, "Algorithms for embedded graphs," 2014. [Online]. Available: http://www.di.ens.fr/~colin/cours/algo-embedded-graphs.pdf
- [30] Li Chen, "Discrete Jordan curve theorem," in Vision Geometry VIII, International Society for Optics and Photonics. SPIE, September 1999, pp. 82–94.
- [31] N. Vandersickel et al., "Directed networks as a novel way to describe and analyze cardiac excitation: Directed graph mapping," Frontiers in Physiology, vol. 10, p. 1138, 2019.
- [32] J. Feher, "The Cardiac Action Potential," in *Quantitative Human Physiology*, 2nd ed. Academic Press, 2012, pp. 528 536.
- [33] R. Cheng, M. Chang, and C. Yuan Ng, "Risks from catheter ablation of atrial fibrillation: A review of methods, efficacy, and safety," *Journal of atrial fibrillation*, vol. 4, no. 6, p. 455, 2012.
- [34] Z. F. Issa, J. M. Miller, and D. P. Zipes, "Molecular Mechanisms of Cardiac Electrical Activity," in *Clinical Arrhythmology and Electrophysiology*, 3rd ed. Elsevier, 2019, pp. 1–14.
- [35] F. Ali and H. Khanzada. (2019) WPW syndrome. Suma Health, Cardiology-Patient Care Conference. [Online]. Available: https://uploads-ssl.webflow.com/5b3e2727cec9e31eaecde40f/ 5da5e25e23aef0cdf72a2463_2019-10-15-Cardiology%20Med% 20D%20Med%20C%20Patient%20Care%20Conference.pdf
- [36] D. Dawson *et al.*, "Linear affine transformations between 3-lead (frank xyz leads) vectorcardiogram and 12-lead electrocardiogram signals," *Journal of Electrocardiology*, vol. 42, no. 6, pp. 622–630, 2009.
- [37] R. Jaros, R. Martinek, and L. Danys, "Comparison of different electrocardiography with vectorcardiography transformations," *Sensors*, vol. 19, no. 14, 2019.
- [38] K. H. Norian, "An electrical model of the heart," *The International Journal of Electrical Engineering & Education*, vol. 45, no. 1, pp. 26–33, 2012.
- [39] R. Clayton *et al.*, "Models of cardiac tissue electrophysiology: Progress, challenges and open questions," *Progress in Biophysics and Molecular Biology*, vol. 104, no. 1, pp. 22–48, 2011.
- [40] N. Sperelakis and T. Hoshiko, "Electrical impedance of cardiac muscle," Circulation Res., vol. 9, no. 6, pp. 1280–1283, 1961.
- [41] A. C. Guyton and J. E. Hall, *Textbook of Medical Physiology*, 11th ed. Saunders Elsevier, 2006.
- [42] R. Klabunde, Cardiovascular physiology concepts. LWW, 2011.



Fariba Ariaei received her BSc and MSc in Mechanical and Aerospace Engineering from Sharif University of Technology, Tehran, Iran. She received her Ph.D. in Electrical Engineering from University of Southern California (USC) in 2008. In 2011, she completed her Postdoctoral Fellowship training at The Johns Hopkins University. She is now an Associate Researcher in the Department of Mechanical and Aerospace Engineering at the University of California, Irvine, and an

Adjunct Lecturer at Viterbi School of Engineering at USC. Her current research focuses on Network Science, Stochastic Dynamical Systems, and Biological Systems.



Zahra Askarzadeh obtained her BS degree in Mechanical Engineering from Sharif University of Technology, Tehran, Iran, in 2015. She is currently a Ph.D. student in Mechanical and Aerospace Engineering at University of California, Irvine.



Yongxin Chen received his BSc from Shanghai Jiao Tong University in 2011 and Ph.D. from University of Minnesota in 2016, both in Mechanical Engineering. He is now an assistant professor in the School of Aerospace Engineering at Georgia Tech. Before joining Georgia Tech in 2018, he served on the faculty at Iowa State University (2017-2018) and prior to that he was for one year a postdoctoral researcher at Memorial Sloan Kettering Cancer Center in New York. He

received the George S. Axelby Best Paper Award in 2017 and the NSF CAREER Award in 2020. His current research focuses on control, machine learning and robotics.



Tryphon T. Georgiou (M'79–SM'99–F'00) was educated at the National Technical University of Athens, Greece (1979) and the University of Florida, Gainesville (PhD. 1983). He is currently a Distinguished Professor at the Department of Mechanical and Aerospace Engineering, University of California, Irvine, CA, USA. Earlier, he served on the faculty of Florida Atlantic University (1983–86), Iowa State University (1986–89), and the University of Minnesota (1989-2016). He is

a recipient of the George S. Axelby Outstanding Paper award of the IEEE Control Systems Society for the years 1992, 1999, 2003, and 2017, a Fellow of the IEEE, SIAM and IFAC, and a Foreign Member of the Royal Swedish Academy of Engineering Sciences (IVA).